# Xenon photoionization in the vicinity of 4*d* giant resonance and Cooper minimum using an XUV-NIR pump-probe experiment

Sonu Kumar,[1,2] Stefan Düsterer,[1] Ulrike Frühling,[1] Skirmantas Alisauskas,[1] Giovanni Cirmi,[1] Marie Kristin Czwalinna,[1] Uwe Große-Wortmann,[1] Nick Kschuev,[1] Frederik Kuschewski,[1,*] Tino Lang,[1] Hannes Lindenblatt,[3] Bastian Manschwetus,[1,†] Severin Meister,[3] Christina C. Papadopoulou,[1] Christopher Passow,[1] Juliane Rönsch-Schulenburg,[1] Nora Schirmel,[1] Sebastian Schulz,[1] Florian Trost,[3] Han Xu,[4] Igor Litvinyuk,[5] Robert Moshammer,[3] Nikolay M. Kabachnik,[4,6] Benjamin Erk,[1] and Atia Tul-Noor[1,‡]

[1]*Deutsches Elektronen-Synchrotron DESY, 22607 Hamburg, Germany*

[2]*Department of Physics, Universität Hamburg, 22607 Hamburg, Germany*

[3]*Max-Planck-Institut für Kernphysik, 69117 Heidelberg, Germany*

[4]*European XFEL GmbH, 22869 Schenefeld, Germany*

[5]*Centre for Quantum Dynamics and Australian Attosecond Science Facility, Griffith University, Nathan, Queensland 4111 Australia*

[6]*Donostia International Physics Center (DIPC), 20018 Donostia/San Sebastian, Spain*

(Received 17 July 2024; accepted 12 November 2024; published 6 December 2024)

The relaxation processes in atomic xenon following core ionization of the 4*d* and 4*p* subshells by extreme ultraviolet (XUV) pulses from a free-electron laser (FLASH) are investigated using ion time-of-flight spectroscopy. We compare the dynamics following ionization and Auger-Meitner decays at 90-eV photon energy, i.e., near the giant resonance, with those at 160 eV, near the Cooper minimum, where cross sections for photoionization of the 4*d* and 4*p* subshells are similar. Final states with charges higher than 4 show signatures of sequential absorption of two XUV photons, followed by subsequent Auger-Meitner decay. The averaged lifetimes of some important excited states are measured in a two-color XUV-pump–near-infrared-probe experiment. A transient enhancement in the ion yield of $Xe^{5+}$ with an average lifetime of $(49 \pm 3)$ fs is obtained, attributed to transient intermediate states following the decay of 4*d* double-core-hole states.

DOI: 10.1103/PhysRevA.110.063104

## I. INTRODUCTION

Inner-shell ionization or excitation of atoms and molecules by the impact of energetic photons creates a core hole, a highly unstable state of matter that undergoes complex decay mechanisms involving correlated electrons, often leading to a dication or higher-charged ions. These short-lived, highly excited states typically relax through either radiative or nonradiative, single or multiple Auger-Meitner (AM) decay [1]. Atomic inner-shell relaxation, therefore, serves as a prime example of complex multiparticle dynamics and has been intensively studied at synchrotrons, high-order harmonic-generation sources (see, e.g., [2,3] and references therein), and, more recently, free-electron lasers (FELs) [4,5]. Xenon is an often studied system for these processes due to its intriguing behavior in the extreme ultraviolet (XUV) domain [6] and significant photoabsorption cross sections. Various techniques have been used, such as multielectron coincidence methods [7], ion-electron coincidence spectroscopy [8], time-resolved multielectron spectroscopy [9], time-of-flight spectrometry [10], and yield measurement of multiply charged ions as a function of incident photon energy [11,12]. Precise ion-yield measurements and known photoionization cross sections allow one to estimate the relative probabilities for the production of multiply charged ions and offer valuable insights into the deexcitation dynamics of an atom with a core hole through AM decays [10,13,14].

Double-core-hole states of Xe, i.e., in the $4d^{-2}$ configuration, have received considerable attention due to their production via strongly correlated 4*p* states [15] as well as their generation from $4s^{-1}$ AM decay [16]. These states were investigated previously using multielectron-ion coincidence spectroscopic methods [17,18], resolving contributions from different ionization pathways. However, detailed information about the temporal order of their relaxation dynamics and pathways is experimentally accessible only through time-domain observation and has remained largely unexplored due to the short lifetimes of these states and the limitations in temporal and instrumental resolution in experiments. Pioneering pump-probe ion-charge-state spectroscopy experiments [19,20] have provided information about the average lifetime of intermediate states at various steps of the AM decay resulting from single-core-hole ionization. Here, we apply a

*Present address: German Aerospace Centre, Institute of Quantum Technologies, 89081 Ulm, Germany.

†Present address: Class 5 Photonics, 22607 Hamburg, Germany.

‡Contact author: atia.tul.noor@desy.de

similar approach to explore the states resulting from both single-core-hole and double-core-hole ionizations and the dynamics of the involved AM decay steps in Xe. Combining a femtosecond, intense XUV pulse from an FEL with a time-synchronized optical laser pulse allows the investigation of fundamental inner-shell photoionization processes in which an XUV pulse triggers the dynamics by inducing a core hole, and a delayed probe pulse is used to trace the inner-shell relaxation dynamics of AM decay. The delayed probe pulse can interact with (short-lived) intermediate states before the decay, promoting ionization and thus altering the charge state of the ion that is finally detected. This technique has already been established, and the dynamics of various processes have been successfully investigated, including ultrafast electronic relaxation of autoionization states [21] and the cascaded decay times of Xe $4d$ core holes [19].

In the present work, we investigate the AM decay of Xe $4d^{-1}$ and $4p^{-1}$ states and their time evolution using ion time-of-flight (TOF) spectroscopy. In the first step, we measured and compared the relative ion yields of multiply charged ions for Xe at two distinct photon energies: one at 90 eV, which served as a benchmark due to the large photoabsorption cross section [22] resulting from the extensively studied giant resonance [6,23–27], and the other at 160 eV in the vicinity of Cooper minimum, where the $4d$ and $4p$ photoionization probabilities experience a pronounced minimum [28]. The resulting charge state distributions for single and double ionization are associated with various AM decay pathways. Subsequently, in a time-resolved XUV-pump near infrared (NIR) probe experiment, we investigated the time evolution of these inner-shell holes and obtain the average lifetimes of transiently populated states. The findings are compared to previously reported results obtained at similar photon energies for 90 eV [6,19].

## II. EXPERIMENT

The experiments were performed at the Free-Electron-Laser in Hamburg (FLASH) on beamline FL26 at the reaction microscope (REMI) end station of the FLASH2 branch [29] at two separate beam times. The pump-probe setup used here is described in detail elsewhere [30]. Briefly, FEL pulses with a photon energy of 90 or 160 eV and a pulse duration of approximately $(20 \pm 10)$ fs full width at half maximum (FWHM) are spatially and temporally overlapped with near-infrared (NIR) pulses [800-nm central wavelength, $(15 \pm 3)$ fs FWHM] from a synchronized laser system, matching the burst-mode pulse pattern of FLASH. The average FEL pulse energy measured by a gas-monitor detector (GMD) [31] is 2 μJ for 160-eV photon energy and 1.5 μJ for 90-eV photon energy, thus yielding a peak intensity on the order of $\sim 10^{13}$ W/cm$^2$. The overall temporal resolution of the experiment is $(46 \pm 5)$ fs (FWHM), determined by fitting an error function to the $Xe^{2+}$ ion yield, as described in detail in [30]. Both beams are focused onto a supersonic gas jet at the center of the REMI. The diameter of the focus spot size of the XUV beam is ~25 μm (FWHM), whereas the focal size of the NIR beam is ~50 μm (FWHM), estimated using a focus camera that mimics the beam profile at the target. The same NIR laser system is used for both beam times.

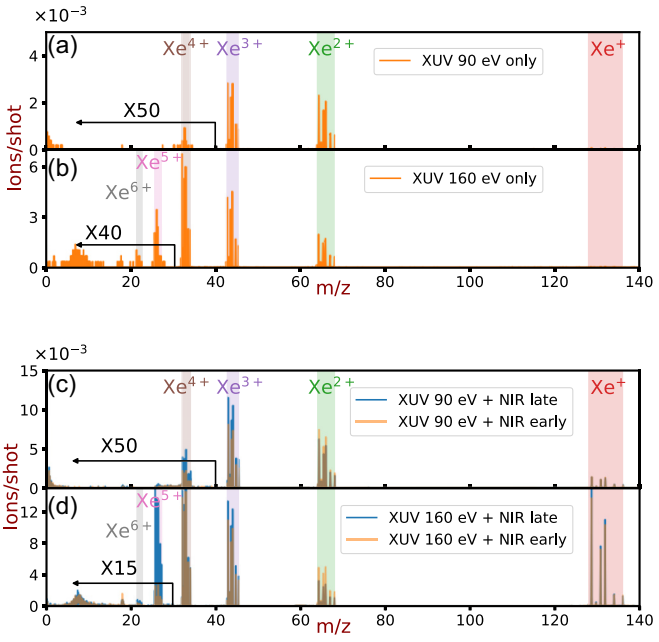


FIG. 1. The mass-to-charge spectra of Xe ions recorded at (a) 90-eV and (b) 160-eV photon energies. The bottom panels show the mass-to-charge spectra with XUV and NIR for 100-fs early and late delays: (c) 90-eV XUV with NIR and (d) 160-eV XUV with NIR. In the low-mass-to-charge regime [below 40 in (a) and (c) and below 30 in (b) and (d)], the ion intensities are multiplied by a factor of (a) 50, (b) 40, (c) 50, and (d) 15 for better visibility. The multipeak structure is due to the distribution of Xe isotopes.

The pump-probe experiments were performed with slightly different parameters, resulting in maximum intensities on target of $\sim 8 \times 10^{13}$ and $\sim 1 \times 10^{14}$ W/cm$^2$ for the measurements using 90- and 160-eV FEL photon energies, respectively. An inaccuracy of ~50% is estimated in determining the respective laser intensities due to the inability to measure the pulse energy and focus size directly in the actual interaction volume.

## III. RESULTS AND DISCUSSION

### A. Mass spectra and relative ion yields at 90 and 160 eV

The mass spectra of multiply charged Xe ions obtained after interaction with only FEL pulses at photon energies of 90 and 160 eV are presented in Figs. 1(a) and 1(b). The multiple peak structures of the individual charge states are due to the natural presence of different Xe isotopes. In the mass spectrum of Xe taken at 90-eV photon energy [Fig. 1(a)], ion signals with $Xe^{q+}$ $(q = 2 - 4)$ are visible. The spectrum closely resembles those observed in previous studies [6,25] under low FEL irradiance conditions. Here, $Xe^{2+}$ is the most abundant peak at 56%, followed by $Xe^{3+}$, comprising 43% [25]. The relative ion yields provide an estimate of the branching ratios, which are the yield of a particular charge state relative to the total yield of all ions for the final-state configuration resulting from the decay of core-hole-excited $Xe^{1+}$. The relative ion yields for 90-eV photon energy are listed in Table I. Figure 2 presents the energy-level scheme and possible transitions involved in generating

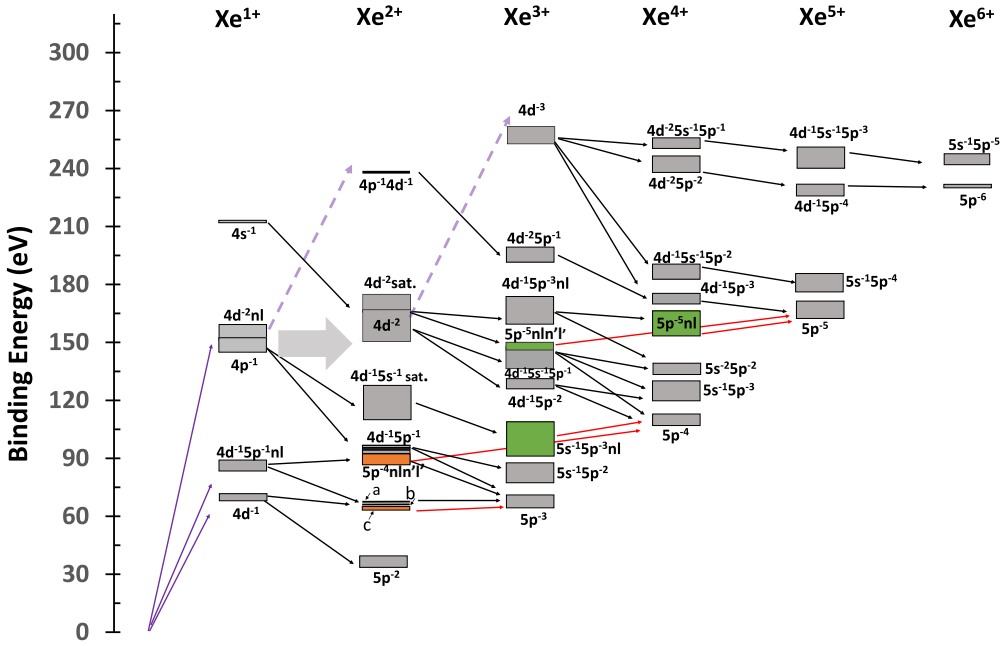


FIG. 2. Energy-level diagram for the $Xe^{q+}$ ($q = 1$–6) most relevant states lying below a binding energy of 320 eV. Atomic Xe is excited or ionized by XUV (purple solid arrow), and subsequent involved AM transitions, the most relevant to the current study, are indicated by black arrows. The gray boxes represent the binding energy range for the states, with AM transitions from the literature [7,8,16,17,32–34]. The light-gray horizontal arrow represents the sCK transition (see text). The green and orange boxes represent the possible states contributing as intermediate states probed by the NIR, indicated by the red arrows. The dashed purple arrow indicates a possible second photon absorption leading to, e.g., the $4d^{-3}$ state.

high-charge states through XUV photoionization, along with probable transitions probed by a NIR laser pulse (discussed later in Sec. III B). The photoionization process for 90 eV is dominated by the single-photon, so-called giant $4d \rightarrow \epsilon f$ continuum resonance. The core-hole excited singly charged $4d^{-1}$ state decays predominantly to $Xe^{2+}$ via a single AM process into the $5p^{-2}$ configuration and to $Xe^{3+}$ via a second AM decay, also known as double AM decay. The AM decay of Xe $4d$ core-hole states ($4d_{3/2}^{-1}$ and $4d_{5/2}^{-1}$) and $4d$ shake-up satellites observed in a $4d^{-1}5p^{-1}nl$ configuration primarily leads to the formation of $Xe^{2+}$ intermediate states. These states are indicated by "a" and "b" in Fig. 2 (presumably the $5s^{-1}5p^{-2}7p$ configuration) located above and "c" lying below the threshold of the $Xe^{3+}$ state (Rydberg series $5s^{-1}5p^{-2}6p$, or the $5p^{-3}nl$ configuration [19]). These intermediate $Xe^{2+}$ states (a and b) sequentially decay to different $Xe^{3+}$ states by a second AM process [24,35]. Additionally, the direct double AM decay also contributes to $Xe^{3+}$ yield in which two electrons are emitted simultaneously (not shown here) [36]. Less than 1% $Xe^{4+}$ is observed at 90 eV, suggesting that the dominant process is single-photon absorption [35].

TABLE I. Relative ion yields of Xe atoms following (a) $4d$ ionization and decay measured at 90-eV photon energy and (b) $4d$ and $4p$ ionization and decay measured at 160-eV photon energy. Yields are given for only XUV, as well as for "early," for which the NIR arrives 100 fs before the FEL, and "late," for which the NIR arrives 100 fs after the FEL, extracted from the ion-yield intensity of the mass-to-charge spectrum in Fig. 1. The measurement uncertainty is on the order of a few percent.

| | XUV | XUV+NIR early | XUV+NIR late |
|---|---|---|---|
| | (a) 90-eV photon energy | | |
| $Xe^{2+}$ | 56% | 60% | 46% |
| $Xe^{3+}$ | 43% | 40% | 54% |
| $Xe^{4+}$ | $\ll$1% | $\leqslant$1% | $\leqslant$1% |
| | (b) 160-eV photon energy | | |
| $Xe^{2+}$ | 29% | 30% | 17% |
| $Xe^{3+}$ | 38% | 38% | 46% |
| $Xe^{4+}$ | 33% | 31% | 34% |
| $Xe^{5+}$ | $\ll$1% | $\leqslant$1% | 3% |
| $Xe^{6+}$ | $\ll$1% | $\ll$1% | $\leqslant$1% |

For ionization with 160-eV photons, higher-charge states have been observed [Fig. 1(b)]. The most abundant species in the mass spectrum is $Xe^{3+}$, followed by $Xe^{4+}$ and $Xe^{2+}$, found to be 38%, 33%, and 29%, respectively (given in Table I). The 160-eV photon energy is high enough to ionize a $4p$ electron (binding energy of 145.6 eV [32]) but well below the threshold of the $4s$ electron (binding energy of 213.32 eV [16]). A single XUV photon can ionize electrons from $4d$ and $4p$ subshells, and subsequent AM decay can produce final charge states of $Xe^{2+}$, $Xe^{3+}$, and $Xe^{4+}$. The $4d$ electron inner-shell ionization cross section at 160 eV is approximately 1 order of magnitude lower than that at 90 eV [22]. Around 180-eV photon energy, the $4d$ cross section shows a distinct minimum, known as the Cooper minimum [15,37]. In the vicinity of this Cooper-minimum region at ~160 eV, the cross sections for $4d$ and $4p$ ionization

are similar [28]. Thus, $Xe^{3+}$ and $Xe^{4+}$ ions are generated predominantly from AM cascades following $4d$ and $4p$ shells ionization. Recent calculations [38] confirmed the reported dominant formation of $Xe^{3+}$ associated with the primary $4p$ photoelectron peak, as identified in a multielectron coincidence study [8]. The potential route to $Xe^{4+}$ involves the population of $4d^{-2}$ states by super-Coster-Kronig (sCK) [15] transition after $4p$ photoionization and subsequent AM decay. Therefore, at 160 eV two independent decay pathways of $4p^{-1}$ and $4d^{-2}$ states must be considered. The vacancy in $4p^{-1}$ can decay through subsequent single and cascaded AM processes and populates mainly $4d^{-1}5p^{-1}$ and $4d^{-1}5s^{-1}$ satellite states $(4d^{-1}5p^{-2}(5d, 6s)^1)$ [32]. The decay pathway of the doubly ionized Xe $4d^{-2}$ state has been investigated through soft x-ray single-photon absorption [17,34], where $Xe^{2+}$ mainly decays to the $Xe^{3+}(4d^{-1}5p^{-2})$ state that further decays to the $5s^{-1}5p^{-3}$ state or the $5p^{-4}$ state of $Xe^{4+}$. The observed large yield of $Xe^{4+}$ compared to that of $Xe^{3+}$ suggests that the channel with ionization and excitation from the $4d^{-2}$ state is dominant and makes a major contribution to the $Xe^{4+}$ formation from subsequent AM decay.

The higher-charge states $Xe^{q+}$ $(q > 4)$ cannot be created with single-photon absorption at 160 eV. The threshold of $Xe^{5+}$ is ∼162.4 eV, and that of $Xe^{6+}$ is ∼230 eV [34] and lies well above the Xe $4p$ binding energy. The presence of these charge states thus indicates a nonlinear photoionization process. The harmonic spectral content of the XUV beam, which is inherent to self-amplified spontaneous emission (SASE) FEL operation, can produce a signal very similar to the nonlinear (sequential) multiphoton absorption through the absorption of a single-photon of double or triple energy. However, the low reflectivity of the beamline mirrors at FL26 for short XUV wavelengths effectively reduces the second- (∼0.0002%) and third-harmonic (∼0.00001%) content by many orders of magnitude compared to the fundamental beam (>60%). Therefore, the contribution of these harmonics can be effectively excluded. Moreover, the ion yield of $Xe^{5+}$ and $Xe^{6+}$ as a function of the XUV pulse intensity (see the Appendix) shows a systematic nonlinear behavior in contrast to $Xe^{2+}$ and $Xe^{3+}$, suggesting that absorption of more than one photon is involved in their generation, most likely via sequential single-photon ionization as the dominant absorption process in the soft x-ray regime [39,40]. Absorption of a second photon in the $4p^{-1}$ state of $Xe^{1+}$ or the $4d^{-2}$ state of $Xe^{2+}$ can result in the $4p^{-1}4d^{-1}$ or $4d^{-3}$ states, respectively. These states can then further decay to $Xe^{5+}$ and $Xe^{6+}$ via possible AM cascade transitions [34,36], as shown in Fig. 2. Additionally, some states of $4d^{-1}5p^{-4}$ in the $Xe^{5+}$ configuration have higher energy than the $5p^{-6}$ state, allowing the AM transition to $Xe^{6+}$. Note that the combined contribution of $Xe^{5+}$ and $Xe^{6+}$ in the relative ion yield is less than 1%.

### B. Delay-dependent ion yield

#### *1. Ionization with 90 eV probed by NIR*

The delay-dependent mass spectra for 90 eV are shown in Fig. 1(c), with the relative ion yields obtained in the pump-probe scheme listed in Table I, where the NIR pulses arriving 100 fs before and after the XUV pulse are called "early" and "late," respectively. The delay range of ±0.5 ps was scanned

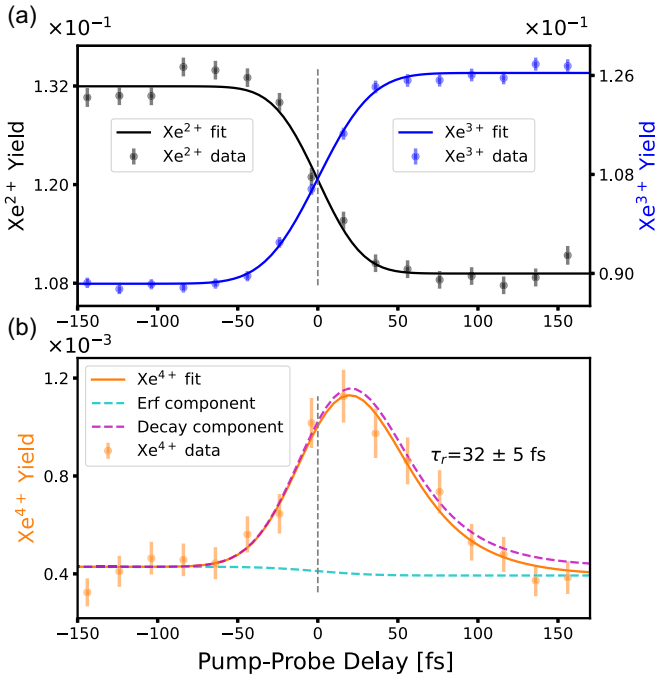


FIG. 3. The ion yields of $Xe^{q+}$ $(q = 2–4)$ as a function of delay between the 90-eV XUV pump and NIR probe pulses. (a) shows the $Xe^{2+}$ (left) and $Xe^{3+}$ (right) yields versus time delay. The ion yield of $Xe^{2+}$ decreases, while $Xe^{3+}$ increases over the same period. The dots and the error bars represent the average and the standard error of the measurement, respectively. The solid black and blue lines are the functions given in Eq. (1) that fit the data, yielding a cross-correlation time of $(30 \pm 3)$ fs for $Xe^{2+}$ and $(37 \pm 2)$ fs for $Xe^{3+}$, respectively. (b) For $Xe^{4+}$, the ion yield versus delay is fitted with an exponential function (see the Appendix and the text), providing an average lifetime of $(32 \pm 5)$ fs. The purple and cyan fits represent the exponential and step function components of the fits, respectively, whereas the solid orange line shows the combined effect of the functions.

back and forth multiple times for each measurement set. For positive delays, the NIR pulse follows the XUV pulse and vice versa. Details of the data analysis and normalization steps are described in the Appendix. Compared to the mass spectrum with only XUV shown in Fig. 1(a), the relative ion yields $Xe^{q+}$ $(q = 2–4)$ for the negative delays are similar. Conversely, for positive delays, the $Xe^{3+}$ yield is enhanced by 25%, and the $Xe^{2+}$ yield drops by 18%, corresponding to the ionization of the $Xe^{2+}$ intermediate states by NIR indicated by the red arrows in Fig. 2. $Xe^{1+}$ is mainly produced by NIR alone. Figure 3 illustrates the delay-dependent ion yields for $Xe^{2+}$, $Xe^{3+}$, and $Xe^{4+}$ recorded at 90 eV. Figure 3(a) shows the $Xe^{2+}$ (left axis) and $Xe^{3+}$ (right axis) ion yields as a function of XUV-NIR delay. For positive delays, a significant decrease is observed in the $Xe^{2+}$ (black dots) signal near zero delays, where pump and probe pulses overlap in time, parallel to a rapid increase in the $Xe^{3+}$ (blue dots) ion yield. The delay-dependent change in the $Xe^{2+}$ yield is due to the creation of a $4d$ core-hole vacancy of $Xe^{1+}$ induced by the XUV, followed by an ultrafast AM decay (lifetime ∼6 fs [41] $\ll \tau_{cc} = 30$ fs cross-correlation time of the pump and probe pulses) that immediately populates intermediate states in $Xe^{2+}$ which are susceptible to the NIR probe pulse. $Xe^{2+}$ is predominantly in

the ground-state $5p^{-2}$ configuration for large positive delays. The laser-induced increase in the $Xe^{3+}$ signal is due to the ionization from the intermediate $Xe^{2+}$ states ($5s^{-1}5p^{-2}6p$ [36] and $5p^{-3}nl$ configuration denoted by c in Fig. 2) with higher binding energies, which are just below the $Xe^{3+}$ threshold and cannot decay spontaneously. These states have a lifetime exceeding ∼100 ps [19,42]. Therefore, the NIR probe pulse, arriving after the XUV pulse, efficiently ionizes these excited intermediate states, leading to a time-dependent increase in the $Xe^{3+}$ yield. The laser-enhanced $Xe^{3+}$ ion yield shows no decrease for large positive delays, as is expected for the long lifetime of the intermediate states compared to the experimental timescale and in agreement with previous measurements [19]. The NIR-induced $Xe^{3+}$ ion yield is predominantly in the ground-state $5p^{-3}$ configuration. For negative delays (i.e., the laser pulse arrives before an inner-shell excitation), the relaxation paths of $4d^{-1}$ and $4d^{-1}5p^{-1}nl$ are minimally affected by the probe pulse. The observed transient features in the $Xe^{2+}$ and $Xe^{3+}$ signals result from the combined effects of the first AM decay and the ionization process induced by NIR, convoluted by the instrument response and finite resolution of the experiment. A Gaussian error function is fitted to the data:

$$f_1(t) = A_0 + A_1\left[1 + \mathrm{erf}\left(\frac{t - t_o}{\tau_{cc}}\right)\right]. \quad (1)$$

Here, $A_0$ represents the baseline signal, and $A_1$ scales the contribution of the error function to the response. The function erf(·) denotes the error function, $t_0$ signifies the center position of the step function, and $\tau_{cc}$ is the cross-correlation time, which is determined by the temporal profiles of the XUV and NIR pulses, residual temporal jitter, and drifts. Here, $\tau_{cc}$ is determined to be (30 ± 3) fs from the $Xe^{2+}$ fit.

At 90-eV photon energy, $Xe^{4+}$ cannot be produced via single-photon absorption (threshold of 106 eV). Less than 1% $Xe^{4+}$ is observed with XUV alone compared to the pump-probe experiment, in which this signal is significantly increased (an increase of about a factor of 2 compared to only XUV). Besides this overall increase, a strong transient feature is also observed in the $Xe^{4+}$ yield. Figure 3(b) shows the $Xe^{4+}$ ion yield as a function of XUV-NIR delay. The signal rises first, followed by a fast decay. The transient increase in the $Xe^{4+}$ ion yield is from the NIR-induced double ionization originating from the doubly excited $5p^{-4}nln'l'$ states of $Xe^{2+}$ (indicated with red arrow in Fig. 2) which are short-lived [19] and decay to $Xe^{3+}$ in the $5p^{-3}$ configuration via a second AM decay [14]. The temporal profiles of the $Xe^{4+}$ ion yield are fitted with a model function that combines the Gaussian error function described in Eq. (1) with an exponential-decay function (see the details in the Appendix). The combined model function is given by

$$f(t) = f_1(t) + A_2 \exp\left(-\frac{(t - t_0)}{\tau_r}\right) \times \left[1 + \mathrm{erf}\left(\frac{(t - t_0)}{\tau_{cc}} - \frac{\tau_{cc}}{2\tau_r}\right)\right] \exp\left(\frac{\tau_{cc}^2}{4\tau_r^2}\right), \quad (2)$$

where $A_2$ scales the contribution of the convoluted error function and exponential decay and $\tau_r$ defines the average lifetime. The fit of the data is shown in Fig. 3(b) (orange solid line) and yields an average lifetime of (32 ± 5) fs, which corresponds to the doubly excited intermediate $Xe^{2+}$ states involved in this decay cascade (mainly $5p^{-4}nln'l'$), in excellent agreement with previous time- and energy-resolved measurements [19,24].

#### 2. *Ionization with 160 eV probed by NIR*

In the case of 160-eV FEL photon energy, ionization from both 4$p$ and 4$d$, with comparable cross sections, alters the branching ratio of the ion yields compared to the 90-eV case. Nonetheless, like for 90 eV, the relative ion yields of charge states $Xe^{q+}$ ($q$ = 2–6) for XUV alone and with pump-probe negative delays remain nearly identical. However, for positive delays, there is a relative decrease in the yield of $Xe^{2+}$ by ∼41%, while those of $Xe^{3+}$ and $Xe^{4+}$ increase by ∼21% and ∼3%, respectively. The most significant relative change is observed in the relative yields of $Xe^{5+}$, increasing by ∼200%, and $Xe^{6+}$, increasing by ∼100%.

Figure 4 presents the ion yield as a function of delay, pumped with 160-eV XUV photons and probed by NIR. Like in Fig. 3(a) (pumped with 90 eV), the ion yield of $Xe^{2+}$ has a steplike dependence on the delay and shows a significant decrease in the vicinity of zero delay, indicating the population of intermediate states that are influenced by the NIR probe, while $Xe^{3+}$ and $Xe^{4+}$ exhibit an increase for large positive delays corresponding to the long lifetime of some of the intermediate states. The $Xe^{3+}$ delay-dependent yield is presumably related to laser ionization of intermediate states after 4$d$ core-hole ionization, as discussed earlier in Sec. III B 1. The overall yield of $Xe^{3+}$ does not change as dramatically compared to 90-eV ionization because at 160 eV a large part of it is generated by the XUV-only signal through the 4$p$ decay process, which is not affected by the NIR. The time-dependent yield of $Xe^{4+}$ can be attributed to the ionization from the intermediate states in the $5s^{-1}5p^{-3}nl$ and $5p^{-4}nl$ configurations (not shown in Fig. 2) of $Xe^{3+}$, which lie below the ionization threshold of $Xe^{4+}$. The ion yield of the $Xe^{3+}$ and $Xe^{4+}$ data is fitted with the function presented in Eq. (1). Essentially, the time evolution of $Xe^{3+}$ and $Xe^{4+}$ includes the contributions from two different origins, 4$d$ and 4$p$, as well as the time comprising both the laser-induced ionization process and AM decay, which cannot be resolved just from the ion-TOF measurement.

The transient feature observed in the $Xe^{5+}$ ion yield as a function of XUV-NIR delay is shown in Fig. 4(c). The yield of $Xe^{5+}$ is increased in the presence of NIR. The signal grows within a few tens of femtoseconds, followed by a longer decay period. The shape of the curve can be explained in terms of various pathways involved in this process. Among the transient states involved in the AM cascades leading to $Xe^{4+}$ and $Xe^{5+}$, there are comparatively long-living states, such as $5p^{-5}nln'l'$, which may be affected by the NIR pulse. The rising edge of the $Xe^{5+}$ yield curve [Fig. 4(c)] may be explained by the double photoionization of the $5p^{-5}nln'l'$ states in $Xe^{3+}$, which results in the formation of $Xe^{5+}$, as indicated by the red arrow in Fig. 2. The decaying part of the $Xe^{5+}$ ion yield can be explained by the competition between the NIR-induced double ionization and AM decay into $Xe^{4+}$

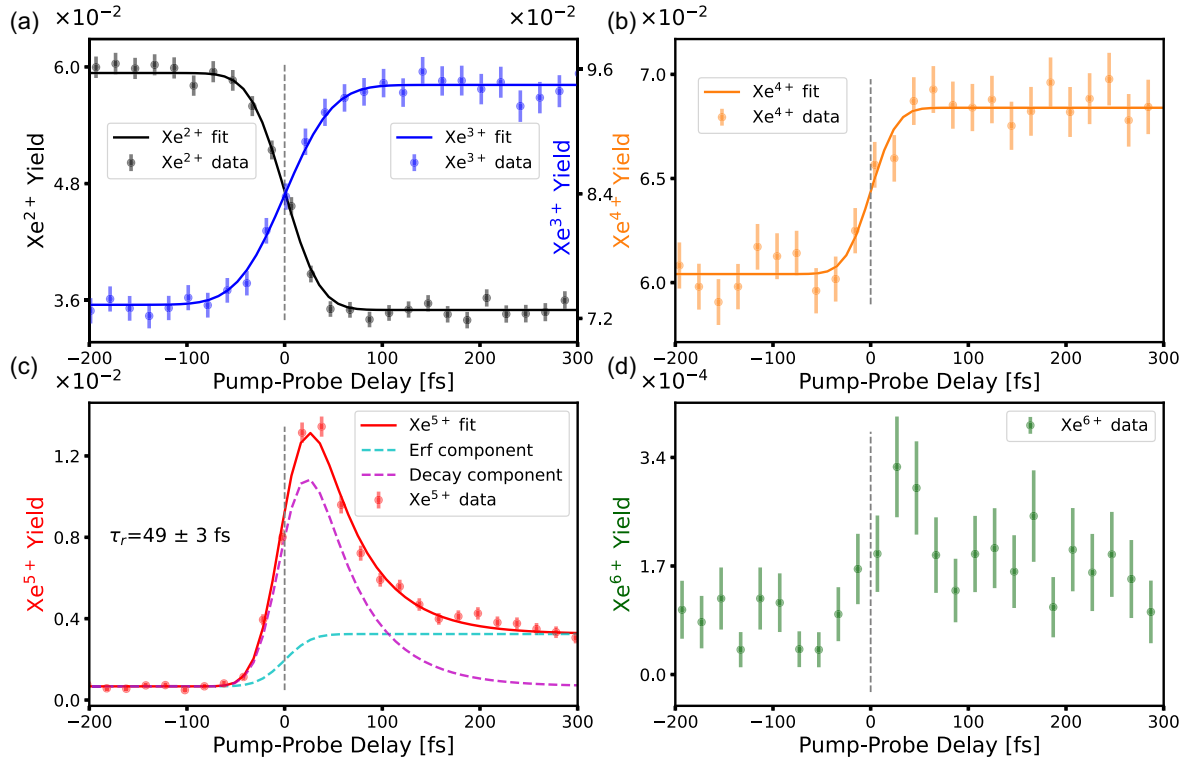


FIG. 4. (a)–(d) The ion yields of $Xe^{q+}(q = 2–6)$ versus delay between the 160-eV XUV pump and NIR probe. In (a) left $y$ axis is for the yield of $Xe^{2+}$, and the right axis is for the yield of $Xe^{3+}$. The ion yields of $Xe^{q+}$ $(q = 2–4)$ are fitted with a step function given in Eq. (1), yielding the cross-correlation time of $(37 \pm 3)$ fs for $Xe^{2+}$, $(44 \pm 5)$ fs for $Xe^{3+}$, and $(31 \pm 7)$ fs for $Xe^{4+}$. The yield of $Xe^{5+}$ in (c) is fitted with the function given in Eq. (2) with a cross-correlation time of $(30 \pm 1)$ fs and an average lifetime of $(49 \pm 3)$ fs. The results of the fitting procedure are described in the text, and more details are given in the Appendix. The purple and cyan fits in (c) represent the exponential and step-function components of the fit, whereas the red solid line shows the combined effect of the function.

(indicated by black arrows in Fig. 2). With increasing delay, the depopulation of these intermediate states by AM decay reduces the ions that can be postionized by the NIR laser, resulting in a decrease in the $Xe^{5+}$ yield for delays $\geqslant 90$ fs. For large positive delays, the enhancement of the ionization yield compared to the negative delays [cyan dashed curve in Fig. 4(c)] suggests that some of the intermediate states (most likely $5p^{-5}nl$) live longer than the experiment's maximum delay range, i.e., 0.5 ps.

To extract the relevant average lifetimes, the experimental data are fitted with the already applied model function for $Xe^{4+}$ in the previously discussed 90-eV case given in Eq. (2). The fit to the measured curve yields an average lifetime of (49±3) fs for the AM decay, which corresponds to the transient intermediate states dominated by $5p^{-5}nln'l'$ involved in this decay cascade. The deduced average lifetime is twice as fast as previously reported in Ref. [43], where the experiment was performed under different conditions with an instrumental response time of ∼120 fs (FWHM).

A different relaxation pathway leads to the generation of $Xe^{6+}$. The ion yield of $Xe^{6+}$ is plotted in Fig. 4(d). The transient feature is observable; however, due to low statistics, it is not possible to deduce any characteristic times. The rising edge near zero delay and the following diminishing of the yield can likely be explained in a manner similar to the $Xe^{5+}$ yield. This involves the population of the ionic states, such as the $5p^{-6}nln'l'$ configuration; their AM decay to $Xe^{5+}$ states; and NIR-induced double ionization leading to the formation of $Xe^{6+}$ ions.

## IV. CONCLUSION

Xe atoms exposed to intense, ultrashort XUV FEL pulses near the Cooper minimum (160 eV) and at the giant $4d$ resonance (90 eV) exhibit different ionization and relaxation processes. The AM transitions following $4d$ single ionization with 90 eV as well as single ionization of $4p$ and double ionization of $4d$ with 160-eV XUV pulses were investigated using ion time-of-flight spectroscopy. The XUV light-intensity dependence of $Xe^{5+}$ and $Xe^{6+}$ ion yield suggested two-photon-induced multiple ionization. AM decay times following the XUV excitation were measured with an improved instrument response time [30] in a two-color XUV pump and NIR probe experiment. The NIR laser probes the transient population of the intermediate excited states before their decay by promoting them to different states, thereby enabling conclusions about intermediate steps in the relaxation pathways leading to different final charge states. The obtained average lifetime of $Xe^{5+}$ $[(49 \pm 3)$ fs] is twice as fast as observed earlier. A different decay channel of $Xe^{6+}$ was observed, most likely arising from NIR-induced double ionization of doubly excited states of $Xe^{4+}$. The present work

demonstrates that utilizing intense XUV and x-ray sources, such as FELs, enables the selective population of core-hole states, and when combined with NIR sources, these setups provide time-domain access to study the dynamics of decay processes in atoms and molecules. A future time-resolved ion-electron coincidence study will help to elucidate the complicated AM decay processes in a state-selective manner and in greater detail. Notably, achieving even higher temporal resolution will be essential to measure some of the AM transitions.

## ACKNOWLEDGMENTS

We acknowledge DESY (Hamburg, Germany), a member of the Helmholtz Association HGF, for providing experimental facilities. Parts of this research were carried out at FLASH2, the REMI end station at beamline FL26, and we would like to thank M. Braune, the machine operators, the run coordinators, and the laser and synchronization teams for their assistance. This research was supported in part through the Maxwell computational resources operated at DESY, Hamburg, Germany. The data were taken in beam time ID No. 11015327 and No. 11010412. N.M.K. acknowledges the financial support from European XFEL and Donostia International Physics Center.

A.T.-N., B.E., S.K., U.F., S.D., B.M., H.L., I.L., S.M., C.C.P., C.P., F.T., T.L., S.A., G.C., and H.X. performed the experiment at the REMI end station. A.T.-N., S.K., B.E., and C.P. processed and analyzed the experimental data. A.T.-N. and S.K. designed the figures. T.L., S.A., G.C., S.K., N.S., and B.M. set the laser parameters, and S.S., N.S., N.K., BM, F.K., T.L., S.A., and U.G.-W. set up the LAM feedback. J.R.-S., M.K.C., and S.D. configured the beam-based-accelerator stabilization and optimized the FEL for short XUV pulses. A.T.-N., S.K., B.E., S.D., U.F., and N.M.K. discussed the data, worked on interpretation, and wrote the first draft of the paper. All authors contributed to the discussions.

## APPENDIX: DATA ANALYSIS

The experiments were performed during two separate beam times, with similar data analysis procedures employed in each case. Data analysis was done in a PYTHON program using standard packages like NUMPY, SCIPY, PANDAS, and MATPLOTLIB. Here, we refer to the experiment conducted at a photon energy of 160 eV. The pump-probe scan is performed by adjusting the delay stage of the NIR laser in steps of 30 fs and recording 25 000 shots at each delay. The TOF and impact position of the ions are detected by time- and position-sensitive detectors. The background is filtered by applying two linear functions, $y = mx + c$, as filters on the $X$-position detector and two constant functions, $y = \pm c$, as filters on the $Y$-position detector, shown in Fig. 5(a) and 5(b). In the postanalysis, data are sorted according to pulse-to-pulse bunch-arrival-monitor [44] values and subtracted from the delay-stage values for jitter correction between pump and probe pulses. The new delay values are averaged into 20-fs-wide bins. The ion yield of Xe charge states is calculated by selecting the regions of interest within the TOF data. For normalization, ion yields were divided by the number of shots.

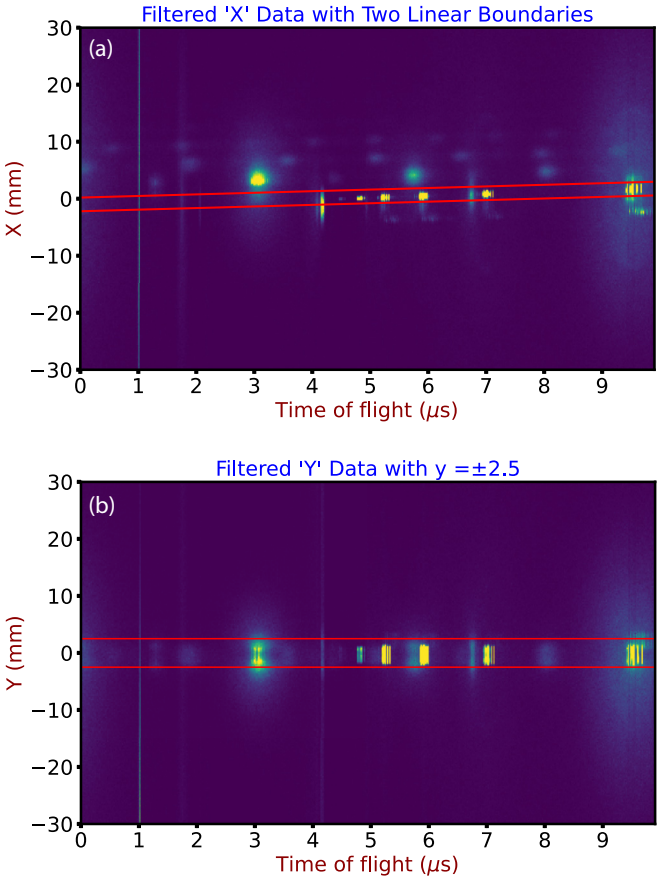


FIG. 5. Filter applied on the $X$ and $Y$ positions of the ion detector, selecting only the data within the ranges indicated by the red lines on (a) the $X$ and (b) $Y$ coordinates, respectively.

Due to the nature of the SASE pulse, there can be significant fluctuations in FEL intensity from one pulse to the next. This is reduced by taking the data only in the 1–5-μJ range and dividing the ion yields by the FEL pulse energy for each pulse.

### 1. Error calculation

The uncertainty of the pump-probe experimental data is determined by Poisson distribution, where the square root of the counts represents the standard deviation associated with a count. Therefore, if $N$ events are measured, the uncertainty (or error) in this measurement is $\sqrt{N}$:

$$E_R = \frac{\sqrt{N}}{N}. \tag{A1}$$

It provides a relative error $E_R$ which measures the error in the size of the count.

### 2. Fitting procedure of pump-probe data

The convolution of two Gaussian pulses is performed to fit the pump-probe data, defined as an integral of the product of the two functions.

$$F(t) = (f \otimes g)(t) = \int_{-\infty}^{\infty} f(t)g(t - t')dt'. \tag{A2}$$

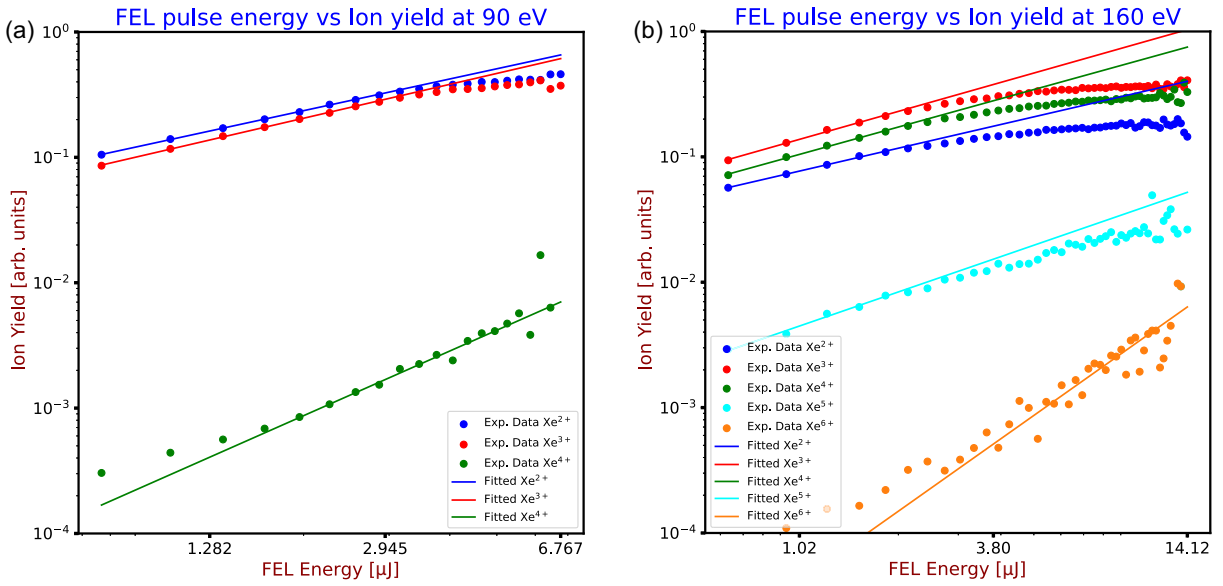


FIG. 6. Ion yield vs FEL pulse energy at the GMD taken at (a) 90 eV and (b) 160 eV.

$g(t)$ is the cross-correlation function between the XUV and NIR pulses, given by

$$g(t) = \exp\left(-\frac{t^2}{\tau_{cc}^2}\right), \tag{A3}$$

where $t$ is the pump-probe delay and $\tau_{cc}$ is the cross-correlation time, given by

$$\tau_{cc}^2 = \frac{\tau_{\text{pump}}^2}{n_{\text{pump}}} + \frac{\tau_{\text{probe}}^2}{n_{\text{probe}}} + \tau_{\text{jitter}}^2, \tag{A4}$$

where $\tau_{\text{pump}}$ and $\tau_{\text{probe}}$ are the pulse durations of the XUV and NIR lasers, respectively; $n_{\text{pump}}$ and $n_{\text{probe}}$ are the number of the photons involved in the process; and $\tau_{\text{jitter}}$ is the timing jitter of two laser systems. $f_1(t)$ represents the atomic response, obtained by convolving the cross-correlation function with a Heaviside $\theta(t)$ function, which yields the error function

$$f_1(t) = \theta(t) \otimes \exp\left(-\frac{t^2}{\tau_{cc}}\right) \propto \left\{\left[1 + \text{erf}\left(\frac{(t-t_0)}{\tau_{cc}}\right)\right]\right\}. \tag{A5}$$

In the case of $Xe^{q+}$ ($q = 2$–4) at 160-eV photon energy and $Xe^{q+}$ ($q = 2$–3) at 90-eV photon energy, the steplike behavior allows fitting using Eq. (A5), which is further simplified to Eq. (1) in the main text. The transient increase results from the product of a step function and exponential decay:

$$f_2(t) \propto \exp\left(-\frac{(t-t_0)}{\tau_r}\right)\left[1 + \text{erf}\left(\frac{(t-t_0)}{\tau_{cc}} - \frac{\tau_{cc}}{2\tau_r}\right)\right] \times \exp\left(\frac{\tau_{cc}^2}{4\tau_r^2}\right). \tag{A6}$$

The transient dynamics in $Xe^{4+}$ and $Xe^{5+}$ with 90 and 160 eV, respectively, are fitted with the function resulting from the linear sum of $f_1(t)$ and $f_2(t)$ that leads to the expression

$$f(t) = A_0 + A_1 f_1(t) + A_2 f_2(t). \tag{A7}$$

For the data shown here, the least-squares fitting is problematic: It has multiple solutions, and most solutions have a large correlation between fitted parameters. Therefore, we used the Metropolis algorithm, which is a standard approach for such a problem. The fitting method and algorithm used in this paper are taken from Ref. [45].

### 3. Ion yield versus FEL intensity

The Xe ion yield is calculated by selecting a region of interest within the TOF condition. The yields of $Xe^{q+}$ ($q = 2$–4) for 90 eV photon energy and $Xe^{q+}$ ($q = 2$–6) for 160-eV photon energy are analyzed as a function of the FEL intensity $I$, as shown in a double-logarithmic plot in Fig. 6. The ion yield versus FEL intensity data are fitted with a linear function, $y \propto I^n$, where the slope $n$ indicates the number of photons absorbed. The green curve fitted to the $Xe^{4+}$ ion yield for 90 eV and the blue and orange curves fitted to $Xe^{5+}$ and $Xe^{6+}$, respectively, for 160 eV show that the slope increases systematically, indicating that more than one photon is involved in their production. The linear relationship for low-charge states at low intensities confirms their main origin from one-photon processes. The saturation of ion signal at high irradiance is due to target depletion.

[1] W. Mehlhorn, 70 years of Auger spectroscopy, a historical perspective, J. Electron Spectrosc. Relat. Phenom. **93**, 1 (1998).

[2] U. Becker and D. A. Shirley, *VUV and Soft X-ray Photoionization* (Plenum Press, New York, 1996).

[3] P. Agostini and L. F. DiMauro, The physics of attosecond light pulses, Rep. Prog. Phys. **67**, 813 (2004).
[4] W. Ackermann *et al.*, Operation of a free-electron laser from the extreme ultraviolet to the water window, Nat. Photon. **1**, 336 (2007).
[5] C. Bostedt, S. Boutet, D. M. Fritz, Z. Huang, H. J. Lee, H. T. Lemke, A. Robert, W. F. Schlotter, J. J. Turner, and G. J. Williams, Linac coherent light source: The first five years, Rev. Mod. Phys. **88**, 015007 (2016).
[6] A. A. Sorokin, S. V. Bobashev, T. Feigl, K. Tiedtke, H. Wabnitz, and M. Richter, Photoelectric effect at ultrahigh intensities, Phys. Rev. Lett. **99**, 213002 (2007).
[7] Y. Hikosaka, Multi-electron–ion coincidence spectrometer with a high-efficiency microchannel plate detector, J. Electron Spectrosc. Relat. Phenom. **255**, 147158 (2022).
[8] Y. Hikosaka, P. Lablanquie, F. Penent, T. Kaneyasu, E. Shigemasa, J. H. D. Eland, T. Aoto, and K. Ito, Single, double, and triple Auger decay of the Xe 4*p* core-hole states, Phys. Rev. A **76**, 032708 (2007).
[9] P. Zhang, J. Trester, K. Ueda, M. Han, T. Balčiūnas, and H. J. Wörner, Time-resolved multielectron coincidence spectroscopy of double Auger-Meitner decay following Xe 4*d* ionization, Phys. Rev. Lett. **132**, 083201 (2024).
[10] N. Saito and I. H. Suzuki, Multiple photoionization in Ne, Ar, Kr and Xe from 44 to 1300 eV, Int. J. Mass Spectrom. Ion Processes **115**, 157 (1992).
[11] T. Hayaishi, T. Matsui, H. Yoshii, A. Higurashi, E. Murakami, A. Yagishita, T. Aoto, T. Onuma, and Y. Morioka, Post-collision interaction effects following 4p-shell ionization of Xe, J. Phys. B **35**, 141 (2002).
[12] T. Hayaishi, A. Yagishita, E. Shigemasa, E. Murakami, and Y. Morioka, Coincidence spectra of threshold electrons and ions around the Kr 3*d* and Xe 4*d* delayed onset regions, Phys. Scr. **41**, 35 (1990).
[13] D. Holland, K. Codling, G. Marr, and J. West, Multiple photoionisation in the rare gases from threshold to 280 eV, J. Phys. B **12**, 2465 (1979).
[14] T. Hayaishi, Y. Morioka, Y. Kageyama, M. Watanabe, I. Suzuki, A. Mikuni, G. Isoyama, S. Asaoka, and M. Nakamura, Multiple photoionisation of the rare gases in the XUV region, J. Phys. B **17**, 3511 (1984).
[15] G. Wendin and M. Ohno, Strong dynamical effects of many-electron interactions in photoelectron spectra from 4*s* and 4*p* core levels, Phys. Scr. **14**, 148 (1976).
[16] Y. Hikosaka and S. Fritzsche, Coster–Kronig and super Coster–Kronig transitions from the Xe 4s core-hole state, Phys. Chem. Chem. Phys. **24**, 17535 (2022).
[17] Y. Hikosaka, P. Lablanquie, F. Penent, T. Kaneyasu, E. Shigemasa, J. H. D. Eland, T. Aoto, and K. Ito, Double photoionization into double core-hole states in Xe, Phys. Rev. Lett. **98**, 183002 (2007).
[18] M. Fushitani *et al.*, Multielectron-ion coincidence spectroscopy of Xe in extreme ultraviolet laser fields: Nonlinear multiple ionization via double core-hole states, Phys. Rev. Lett. **124**, 193201 (2020).
[19] M. Uiberacker *et al.*, Attosecond real-time observation of electron tunnelling in atoms, Nature (London) **446**, 627 (2007).
[20] T. Uphues, M. Schultze, M. Kling, M. Uiberacker, S. Hendel, U. Heinzmann, N. M. Kabachnik, and M. Drescher, Ion-charge-state chronoscopy of cascaded atomic Auger decay, New J. Phys. **10**, 025009 (2008).
[21] M. Drescher, M. Hentschel, R. Kienberger, M. Uiberacker, V. Yakovlev, A. Scrinzi, T. Westerwalbesloh, U. Kleineberg, U. Heinzmann, and F. Krausz, Time-resolved atomic inner-shell spectroscopy, Nature (London) **419**, 803 (2002).
[22] U. Becker, D. Szostak, H. G. Kerkhoff, M. Kupsch, B. Langer, R. Wehlitz, A. Yagishita, and T. Hayaishi, Subshell photoionization of Xe between 40 and 1000 eV, Phys. Rev. A **39**, 3902 (1989).
[23] M. G. Makris, P. Lambropoulos, and A. Mihelič, Theory of multiphoton multielectron ionization of xenon under strong 93 eV radiation, Phys. Rev. Lett. **102**, 033002 (2009).
[24] F. Penent, J. Palaudoux, P. Lablanquie, L. Andric, R. Feifel, and J. H. D. Eland, Multielectron spectroscopy: The xenon 4*d* hole double Auger decay, Phys. Rev. Lett. **95**, 083002 (2005).
[25] M. Richter, M. Y. Amusia, S. V. Bobashev, T. Feigl, P. N. Juranić, M. Martins, A. A. Sorokin, and K. Tiedtke, Extreme ultraviolet laser excites atomic giant resonance, Phys. Rev. Lett. **102**, 163002 (2009).
[26] N. Gerken, S. Klumpp, A. A. Sorokin, K. Tiedtke, M. Richter, V. Bürk, K. Mertens, P. Juranić, and M. Martins, Time-dependent multiphoton ionization of xenon in the soft-x-ray regime, Phys. Rev. Lett. **112**, 213002 (2014).
[27] J. Viefhaus, M. Braune, S. Korica, A. Reinköster, D. Rolles, and U. Becker, Auger cascades versus direct double Auger: Relaxation processes following photoionization of the Kr 3d and Xe 4d, 3d inner shells, J. Phys. B **38**, 3885 (2005).
[28] D. W. Lindle, T. A. Ferrett, P. A. Heimann, and D. A. Shirley, Photoemission from Xe in the vicinity of the 4*d* Cooper minimum, Phys. Rev. A **37**, 3808 (1988).
[29] G. Schmid *et al.*, Reaction microscope endstation at FLASH2, J. Synchrotron Radiat. **26**, 854 (2019).
[30] Atia-Tul-Noor *et al.*, Sub-50 fs temporal resolution in an FEL-optical laser pump-probe experiment at FLASH2, Opt. Express **32**, 6597 (2024).
[31] A. A. Sorokin, Y. Bican, S. Bonfigt, M. Brachmanski, M. Braune, U. F. Jastrow, A. Gottwald, H. Kaser, M. Richter, and K. Tiedtke, An X-ray gas monitor for free-electron lasers, J. Synchrotron Radiat. **26**, 1092 (2019).
[32] S. Heinäsmäki, H. Aksela, J. Nikkinen, E. Kukk, A. Kivimäki, S. Aksela, and S. Fritzsche, Lifetime and Auger decay of strongly correlated 4p hole states of xenon, J. Electron Spectrosc. Relat. Phenom. **137–140**, 281 (2004).
[33] S. Svensson, B. Eriksson, N. Mårtensson, G. Wendin, and U. Gelius, Electron shake-up and correlation satellites and continuum shake-off distributions in X-Ray photoelectron spectra of the rare gas atoms, J. Electron Spectrosc. Relat. Phenom. **47**, 327 (1988).
[34] V. Jonauskas, L. Partanen, S. Kučas, R. Karazija, M. Huttula, S. Aksela, and H. Aksela, Auger cascade satellites following 3d ionization in xenon, J. Phys. B: At. Mol. Opt. Phys. **36**, 4403 (2003).
[35] T. Luhmann, C. Gerth, M. Groen, M. Martins, B. Obst, M. Richter, and P. Zimmermann, Final ion-charge resolving electron spectroscopy for the investigation of atomic photoionization processes: Xe in the region of the $4\vec{d}\,\varepsilon f$ resonance, Phys. Rev. A **57**, 282 (1998).
[36] L. Partanen, R. Sankari, S. Osmekhin, Z. Hu, E. Kukk, and H. Aksela, Multiple ionization of Xe—comparison of

de-excitation pathways following $3d_{5/2}$ ionization and $3d_{5/2}\rightarrow 6p$ resonance excitation, J. Phys. B: At. Mol. Opt. Phys. **38**, 1881 (2005).

[37] J. W. Cooper, Photoionization from outer atomic subshells. A model study, Phys. Rev. **128**, 681 (1962).

[38] Z. Liu, Q. Liu, Y. Ma, F. Zhou, and Y. Qu, Multiple Auger decay following $Xe^+$ $(4p_{3/2}^{-1})$ ionization, Chin. Phys. Lett. **38**, 023201 (2021).

[39] L. Young *et al.*, Femtosecond electronic response of atoms to ultra-intense x-rays, Nature (London) **466**, 56 (2010).

[40] N. Rohringer and R. Santra, X-ray nonlinear optical processes using a self-amplified spontaneous emission free-electron laser, Phys. Rev. A **76**, 033416 (2007).

[41] S. Fritzsche, A. Grum-Grzhimailo, E. Gryzlova, and N. Kabachnik, Sequential two-photon double ionization of the 4d shell in xenon, J. Phys. B: At. Mol. Opt. Phys. **44**, 175602 (2011).

[42] D. Rolles, R. Boll, B. Erk, D. Rompotis, and B. Manschwetus, An experimental protocol for femtosecond NIR/UV-XUV pump-probe experiments with free-electron lasers, J. Visualized Exp **140**, e57055 (2018).

[43] M. Krikunova *et al.*, Time-resolved ion spectrometry on xenon with the jitter-compensated soft x-ray pulses of a free-electron laser, New J. Phys. **11**, 123019 (2009).

[44] A. Angelovski *et al.*, Evaluation of the cone-shaped pickup performance for low charge sub-10 fs arrival-time measurements at free electron laser facilities, Phys. Rev. Spec. Top. Accel. Beams **18**, 012801 (2015).

[45] D. S. Tikhonov, D. Garg, and M. Schnell, Inverse problems in pump–probe spectroscopy, Photochem **4**, 57 (2024).